INSILI 2 (2026) 100287

Contents lists available at ScienceDirect

In Silico Research in Biomedicine

journal homepage: www.sciencedirect.com/journal/in-silico-research-in-biomedicine

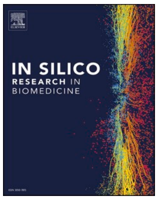

Research Paper

Investigation of bioactive properties, structural, electronic, reactivity analysis and quantum-based characterization of hexadecanamide

G. Revathi [a], P. Rajesh [a,*], S. Kayashrini [a], S. Bala Abirami [b]

[a] *Department of Physics, School of Basic Science, Vels Institute of Science and Technology & Advanced Studies, Pallavaram, Chennain 600117, Tamilnadu, India*

[b] *Department of Condensed Matter Physics, Saveetha School of Engineering, Saveetha Institute of Medical and Technical Sciences (SIMATS), Chennai 602105, Tamil Nadu, India*

ARTICLE INFO

Keywords:
NBO
HDA
RDG
QSPR
Docking

ABSTRACT

Hexadecanamide (HDA), a long-chain fatty acid amide, was identified as a key bioactive constituent in the extract of *Aegle marmelos* using GC-MS analysis and chosen for further theoretical and biological studies. Density functional theory (DFT) was used to examine the molecular structure and vibrational properties of HDA at the B3LYP/6-311++G(d,p) level. The computed results were compared with the experimental FT-IR and UV-visible spectra. The structural stability of the molecule was confirmed by the optimized geometrical parameters, which showed good agreement with the available experimental data. To comprehend the chemical reactivity and stability of HDA, the electronic properties, such as HOMO–LUMO energies, energy gap, chemical hardness, softness, and electrophilicity index, were assessed. Charge delocalization and intramolecular interactions were examined using Natural Bond Orbital (NBO) analysis, and electrophilic and nucleophilic reactive sites were identified using the Molecular Electrostatic Potential (MEP) surface. The theoretical and experimental UV-Vis absorption bands correlated well, according to TD-DFT calculations. The binding affinity of HDA with the target protein was further investigated by molecular docking studies, which revealed advantageous interactions through hydrophobic and hydrogen bonding contacts. HDA's potential as a bioactive therapeutic candidate is supported by the combined experimental and computational results, which indicate that it has strong structural stability and encouraging biological activity.

Introduction

The carboxamide produced from palmitic acid is HDA, a fatty amide. It is functionally related to a Hexadecanoic acid. HDA is a member of a significant class of cell signalling lipids and is a main fatty acid amide that is produced from palmitic acid [1]. This compound's pharmacological relevance is yet unknown, although in a maximum electroshock seizure test in mice, it was found to exhibit a mild anticonvulsant effect when compared to the endocannabinoid palmitoyl ethanolamide [2]. HDA is a major fatty acid amide that is derived from palmitic acid and belongs to an important class of cell signalling lipids. Although the pharmacological significance of this molecule is yet unknown, in a mouse maximal electroshock seizure test, it was found to have a modest anticonvulsant effect in comparison to the endocannabinoid palmitoyl ethanolamide. The molecular structure of pharmaceuticals determines their bioactivity and safety characteristics. Numerous drugs with exceptional safety and effectiveness characteristics are needed by the pharmaceutical and medical sectors. When searching for new medications, it is crucial to design them based on structures. Therefore, evaluating the chemical and physical aspects of structures and establishing the relationship between structure and activity are essential phases in the drug design process. Numerous theoretical and experimental methods are currently used to study biological systems, and their uses are still growing [3,4].

To our knowledge, no one has conducted a full theoretical examination of (HDA) employing density functional theory (DFT) in conjunction with experimental spectroscopic and molecular docking studies. The HDA found in the GC-MS analysis of the *Aegle marmelos* extract was chosen for in-depth structural, electronic, and biological study in this work. Using the B3LYP/6-311++G(d,p) technique, the molecular geometry, vibrational frequencies, and electronic characteristics were examined and correlated with the experimental FT-IR and UV-Vis spectra. The electronic transitions were interpreted and the measured absorption bands were validated using time-dependent DFT

---

* Corresponding author.
E-mail address: rajesh.ncc5coy@gmail.com (P. Rajesh).

https://doi.org/10.1016/j.insi.2026.100287
Received 24 November 2025; Received in revised form 9 March 2026; Accepted 11 March 2026

(TD-DFT) computations. Charge transfer and intramolecular interactions were investigated using Natural Bond Orbital (NBO) analysis, and the chemically reactive areas of the molecule were identified using the Molecular Electrostatic Potential (MEP) surface. Furthermore, HDA's binding behaviour with a biological target was investigated by molecular docking studies, which shed light on the potential mechanism of action. The overall goal of this integrated experimental–theoretical approach is to determine the structure property activity link for HDA and evaluate its potential as a molecule with biological activity.

Methodology

Experimental details

Using a Shimadzu QP2010 Plus, the Aegle marmelos extract was subjected to GC–MS analysis. Several phytochemical constituents were found in the analysis; hexadecanamide (HDA) was chosen for additional theoretical (FT-IR and UV-Vis) and biological studies because of its purported anticancer potential [5]. A PerkinElmer LAMBDA-25 double-beam spectrophotometer with DMSO-d^2 as the solvent was used to record the UV–Vis spectra of the chosen compound at room temperature in the wavelength range of 200–400 nm. Using glowbar sources and KBr beam splitters, PerkinElmer Spectrum FT-IR spectrophotometers were used to acquire the FT-IR spectra in the 4000–400 cm^{-1} range with a resolution of 4 cm^{-1} [6,7]. Every experimental analysis was carried out at SRM University in Tamil Nadu, India's Kattankulathur, Chengalpattu district.

Density functional theory (DFT) calculations

The theoretical and experimental structural data of the molecule were compared. On HDA, molecular docking investigations as well as a number of orbital assessment methods are carried out, including FT-IR, UV-Vis, DFT, HOMO-LUMO, MEP, and NBO [8]. The DFT tools, such as Gaussian 09 W and Gauss View, were used to calculate the ideal skeleton parameters of the structure, and the VEDA software was also used to estimate the PED values in order to carry out the conformational analysis [9]. The ELF, LOL, and RDG were estimated using Multiwfn software. The non-covalent interaction's localization of the electrons was confirmed using Multiwfn and VMD software. Autodock 1.5.6 was used for the molecular docking in order to study the ligand-protein binding behaviour [10].

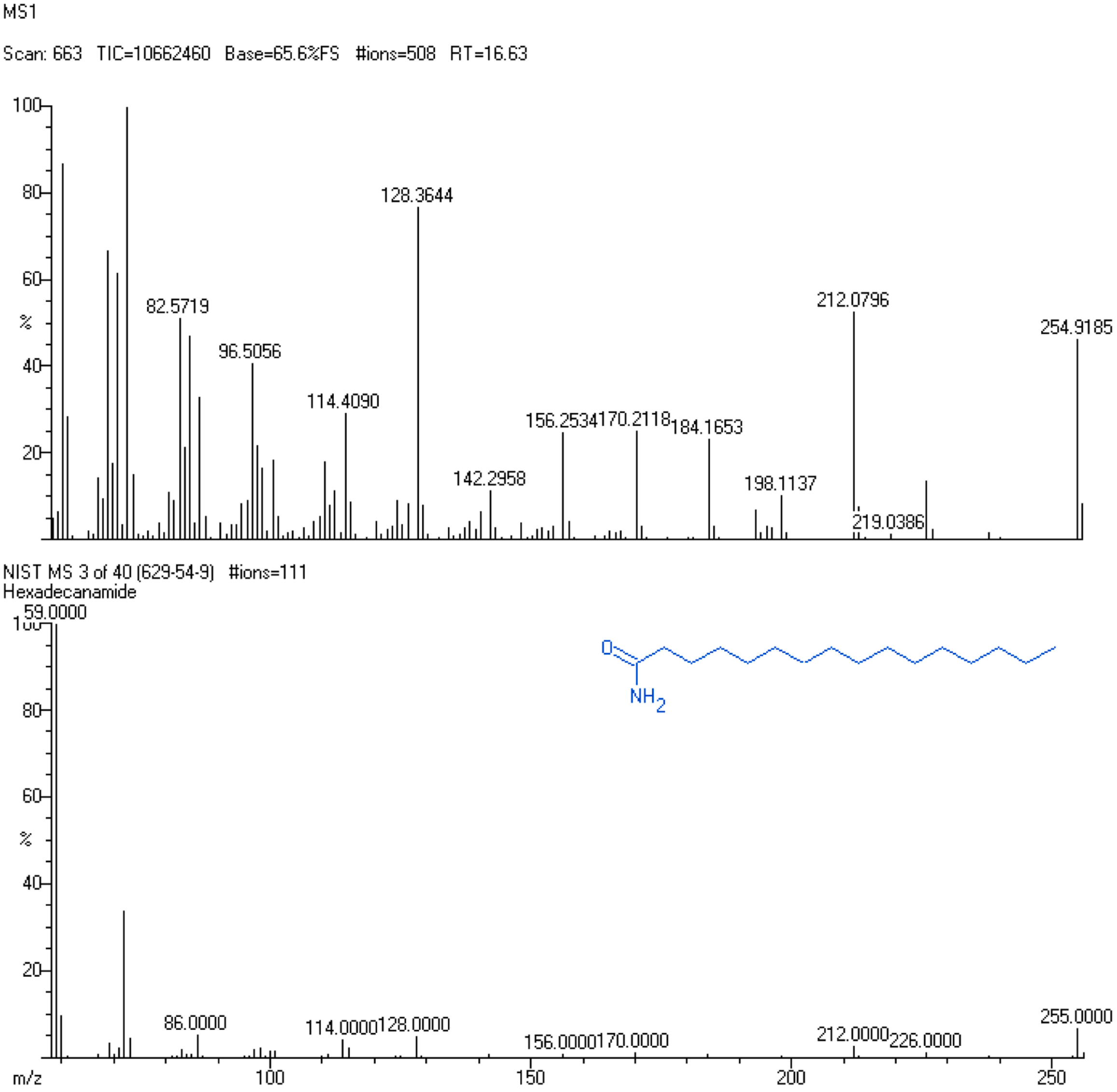

Fig. 1. GC-MS Analysis on HDA.

Result and discussion

GC-MS analysis

The presence of a significant bioactive compound was indicated by the prominent peak at a retention time of 16.63 min shown Fig. 1. in the GC–MS analysis of the extract of HDA. The NIST 14 Mass Spectral Library and the corresponding mass spectrum were compared, and the compound was found to be HDA with a high degree of similarity [11]. The molecular weight of the compound was confirmed by the appearance of the molecular ion peak at m/z 255. The amide functional group and alkyl chains were sequentially cleaved at m/z 82.57, 96.50, 114.40, 128.36, 142.29, 156.25, 170.21, 184.16, 198.11, 212.07, 219.03, and 254.91, as indicated by the mass fragmentation pattern. A stable amide fragment was represented by the base peak, which was detected at m/z 128.36 [12]. HDA structural stability is confirmed by the fragmentation behaviour, which is in line with that of long-chain fatty acid amides. Numerous biological activities, such as anti-inflammatory, antioxidant, antimicrobial, and anticancer effects, are well-known for this compound [13].

Optimized structure

The molecular weight, 255.44 g/mol, and the chemical formula, $C_{16}H_{33}N_{O}$ [14,15]. The 3D structure is a linear chain with a polar amide group on one end, but the 2D structure is CH3(CH2)14CONH2. The alkyl chain gives the molecule its distinctive zigzag form. Its functional groups and achiral alkyl chain (C16H33) are connected to the main amide (-CONH2), suggesting the lack of stereo centres. According to crystal structure, the unit cell dimensions of the orthorhombic crystal system are a = 7.42 Å, b = 8.14 Å, and c = 24.61 Å. It belongs to the Pbca space group. The Chemical and Physical Properties of Hexadecane Density: 0.94 grams/cm^3; index of refraction: 1.44: boiling point: 345 °C (653 °F) at 760 mmHg; flash point: 162 °C (324 °F); autoignition temperature: 380 °C (716 °F). HDA is a fatty acid amide that is derived from HDA acid, also known as palmitic acid. Another name for it is palmitamide. This substance is a member of the long-chain fatty acid amides class of organic compounds. These substances may have roles in signalling, especially in the neurological system, and are frequently physiologically active. It often manifests physically as a solid or powder that is white to off-white in colour it shows in the Fig. 2. In general, it is insoluble in water but soluble in organic solvents like acetone, chloroform, and alcohols. Typically, it has a melting point of 96 to 98 °C. Geometrical parameters like bond length and bond angle are calculated using the Gaussian 09 programmed by the DFT/B3LYP technique and the 6-311++G(d,p) basis set. The improved structural parameters are displayed in Table 1. The functioning of the molecule is largely dependent on the amide Group (-CONH₂). A carbonyl group (C=O) is present, along with bond lengths of 1.2229 Å and 1.3668 Å for C1-O17 and C1-N18 respectively, attached to nitrogen atoms (NH₂) in N18-H50 and N18-H51, which have similar values of 1.0084 Å and 1.0055 Å. The bond angle of the amide is demonstrated by the following combinations: O17-C1-N18, C2-C1-O17, C2-C1-N18, C1-N18-H50, and C1-N18-H51, with corresponding angles of 121.09°, 121.09°,116.98°, 117.55° and 123.23°. Because of its ability to establish hydrogen bonds, this nitrogen gives amides characteristics like solubility in polar liquids. Sixteen carbon atoms that are completely saturated with hydrogen atoms make up the alkyl chain. It has a structure similar to that of a normal fatty acid tail and is nonpolar and hydrophobic. In many different ways, the alkyl group that is joined to the amide group functions as a significant bioactive component [16–18]. The CC, CH, CH2 and CH3 bond length and bond angles found in long-chain fatty acids explain the covalent and ionic bonding as well as the stability of the chemical. The table shows the bond lengths for C1-C2 and C2-H19, which are 1.53 Å and 1.09 Å, respectively, and the bond angles for C1-C2-C3, C1-C2-H19, and H19-C2-H20, which are 118.68°, 105.73° and 105.35°.

Mulliken population analysis

In order to determine the atomic charges in molecular systems and gain an important understanding of their electrical structure and reactive behavior, Mulliken Population Analysis is a commonly utilized technique [19]. Understanding the chemistry of a molecule depends on important molecular features, including vibrational spectra, polarizability, and dipole moment, all of which are influenced by these atomic charges. The electron density in this analysis is divided by the contributions of atoms to molecular orbitals, and Mulliken charges are computed based on the distribution of electrons across atomic orbitals. The calculated Mulliken charges of HDA at a particular theory level and basis set provide important information about the electron distribution in the molecule [20]. The Mulliken charges for each atom are listed in Table 2, which also highlights the regions of electron deficit or richness that may be indicative of possible sites for nucleophilic or electrophilic processes. With a positive charge of 0.56962, the carbon atom at position C_1 is electron-deficient and hence a possible target for nucleophilic attack. Atoms having negative charges, such as C_2 (-0.24055) and C_{16} (-0.30775), on the other hand, may interact with electrophilic species more frequently. Similarly, the nitrogen atom N_{18} is an attractive target for electrophilic attacks because of its large negative charge of -0.62023, which denotes a high electron density surrounding the nitrogen. The oxygen atom O_{17} also exhibits a significant negative charge (-0.51046), an indication of strong electronegativity that suggests that it may be used as an electron donor site in electrophilic processes. Little positive charges are seen across the hydrogen atoms, with H_{19} (0.131212) and

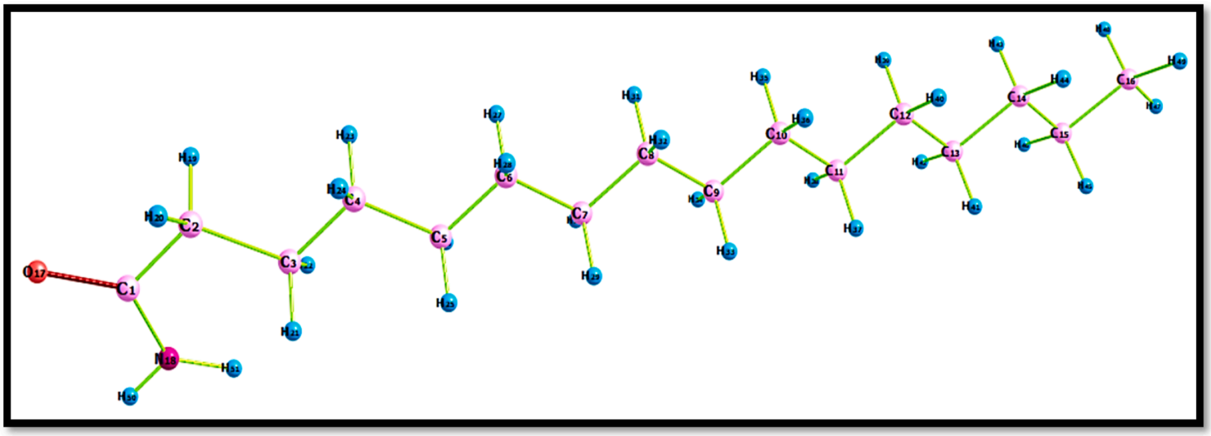

Fig. 2. Optimized molecular structure of HDA.

Table 1

Bond length and bond angle of HDA.

Bond length (Å)	B3LYP/6-311++G (d, p)	Bond length (Å)	B3LYP/6-311++G (d, p)	Bond length (Å)	B3LYP/6-311++G (d, p)
C_1-C_2	1.530	C_6-H_{28}	1.099	C_{12}-H_{39}	1.099
C_1-O_{17}	1.222	C_7-C_8	1.533	C_{12}-H_{40}	1.099
C_1-N_{18}	1.366	C_7-H_{29}	1.099	C_{13}-C_{14}	1.533
C_2-C_3	1.533	C_7-H_{30}	1.099	C_{13}-H_{41}	1.099
C_2-H_{19}	1.096	C_8-C_9	1.533	C_{13}-H_{42}	1.099
C_2-H_{20}	1.096	C_8-H_{31}	1.099	C_{14}-C_{15}	1.533
C_3-C_4	1.534	C_8-H_{32}	1.099	C_{14}-H_{43}	1.099
C_3-H_{21}	1.099	C_9-C_{10}	1.533	C_{14}, H_{44}	1.099
C_3-H_{22}	1.099	C_9-H_{33}	1.099	C_{15}-C_{16}	1.531
C_4-C_5	1.533	C_9-H_{34}	1.099	C_{15}-H_{45}	1.098
C_4-H_{23}	1.098	C_{10}-C_{11}	1.533	C_{15}-H_{46}	1.098
C_4-H_{24}	1.098	C_{10}-H_{35}	1.099	C_{16}-H_{47}	1.094
C_5-C_6	1.533	C_{10}-H_{36}	1.099	C_{16}-H_{48}	1.096
C_5-H_{25}	1.099	C_{11}-C_{12}	1.533	C_{16}-H_{49}	1.096
C_5-H_{26}	1.099	C_{11}-H_{37}	1.099	N_{18}-H_{50}	1.008
C_6-C_7	1.533	C_{11}-H_{38}	1.099	N_{18}-H_{51}	1.005
C_6-H_{27}	1.099	C_{12}-C_{13}	1.533		
Bond Angle (°)	**B3LYP/6-311++G(d, p)**	**Bond Angle (°)**	**B3LYP/6-311++G(d, p)**	**Bond Angle (°)**	**B3LYP/6-311++G(d, p)**
C_2-C_1-O_{17}	121.09	H_{27}-C6-H_{28}	105.93	C_{11}-C_{12}-H_{39}	109.25
C_2-C_1-N_{18}	116.98	C_6-C_7-C_8	113.53	C_{11}-C_{12}-H_{40}	109.25
O_{17}-C_1-N_{18}	121.92	C_6-C_7-H_{29}	109.27	C_{13}-C_{12}-H_{39}	109.26
C_1-C_2-C_3	118.68	C_6-C_7-H_{30}	109.27	C_{13}-C_{12}-H_{40}	109.26
C_1-C_2-H_{19}	105.73	C_8-C_7-H_{29}	109.27	H_{39}-C_{12}-H_{40}	105.90
C_1-C_2-H_{20}	105.72	C_8-C_7-H_{30}	109.27	C_{12}-C_{13}-C_{14}	113.60
C_3-C_2-H_{19}	110.21	H_{29}-C_7-H_{30}	105.93	C_{12}-C_{13}-H_{41}	109.26
C_3-C_2-H_{20}	110.21	C_7-C_8-C_9	113.61	C_{12}-C_{13}-H_{42}	109.26
H_{19}-C_2-H_{20}	105.35	C_7-C_8-H_{31}	109.24	C_{14}-C_{13}-H_{41}	109.25
C_2-C_3-C_4	112.67	C_7-C_8-H_{32}	109.24	C_{14}-C_1-H_{42}	109.25
C_2-C_3-H_{21}	109.84	C_9-C_8-H_{31}	109.26	H_{41}-C_{13}-H_{42}	105.90
C_2-C_3-H_{22}	109.84	C_9-C_8-H_{32}	109.26	C_{13}-C_{14}-H_{15}	113.64
C_4-C_3-H_{21}	108.77	H_{31}-C_8-H_{32}	105.91	C_{13}-C_{14}-H_{43}	109.30
C_4-C_3-H_{22}	108.77	C_8-C_9-C_{10}	113.56	C_{13}-C_{14}-H_{44}	109.30
H_{21}-C_3-H_{22}	106.74	C_8-C_9-H_{33}	109.27	C_{15}-C_{14}-H_{43}	109.20
C_3-C_4-C_5	113.55	C_8-C_9-H_{34}	109.27	C_{15}-C_{14}-H_{44}	109.20
C_3-C_4-H_{23}	109.12	C_{10}-C_9-H_{33}	109.26	H_{43}-C_{14}-H_{44}	105.89
C_3-C_4-H_{24}	109.12	C_{10}-C_9-H_{34}	109.26	C_{14}-C_{15}-C_{16}	113.27
C_5-C_4-H_{23}	109.38	H_{33}-C_9-H_{34}	105.91	C_{14}-C_{15}-H_{45}	109.19
C_5-C_4-H_{24}	109.38	C_9-C_{10}-C_{11}	113.62	C_{14}-C_{15}-H_{46}	109.19
H_{23}-C_4-H_{24}	105.99	C_9-C_{10}-H_{35}	109.25	C_{16}-C_{15}-H_{45}	109.47
C_4-C_5-C_6	113.44	C_9-C_{10}-H_{36}	109.24	C_{16}-C_{15}-H_{46}	109.47
C_4-C_5-H_{25}	109.30	C_{11}-C_{10}-H_{35}	109.26	H_{45}-C_{15}-H_{46}	105.95
C_4-C_5-H_{26}	109.30	C_{11}-C_{10}-H_{36}	109.26	C_{15}-C_{16}-H_{47}	111.51
C_6-C_5-H_{25}	109.26	H_{35}-C_{10}-H_{36}	105.90	C_{15}-C_{16}-H_{48}	111.18
C_6-C_5-H_{26}	109.26	C_{10}-C_{11}-C_{12}	113.58	C_{15}-C_{16}-H_{49}	111.18
H_{25}-C_5-H_{26}	105.98	C_{10}-C_{11}-H_{37}	109.26	H_{47}-C_{16}-H_{48}	107.65
C_5-C_6-C_7	113.59	C_{10}-C_{11}-H_{38}	109.26	H_{47}-C_{16}-H_{49}	107.65
C_5-C_6-H_{27}	109.23	C_{12}-C_{11}-H_{37}	109.26	H_{48}-C_{16}-H_{49}	107.45
C_5-C_6-H_{28}	109.23	C_{12}-C_{11}-H_{38}	109.26	C_1-N_{18}-H_{50}	117.55
C_7-C_6-H_{27}	109.27	H_{37}-C_{11}-H_{38}	105.91	C_1-N_{18}-H_{51}	123.23

Table 2

Mulliken Population Analysis of HDA.

Atoms	Charges (e) (e=1.602 × 10^{-19} C)	Atoms	Charges (e) (e=1.602 × 10^{-19} C)	Atoms	Charges (e) (e=1.602 × 10^{-19} C)
C_1	0.56962	N_{18}	-0.62023	H_{35}	0.084623
C_2	-0.24055	H_{19}	0.131212	H_{36}	0.084631
C_3	-0.21529	H_{20}	0.131214	H_{37}	0.08432
C_4	-0.17304	H_{21}	0.098289	H_{38}	0.084326
C_5	-0.17066	H_{22}	0.098285	H_{39}	0.084626
C_6	-0.16895	H_{23}	0.091838	H_{40}	0.084634
C_7	-0.16861	H_{24}	0.09185	H_{41}	0.08482
C_8	-0.16841	H_{25}	0.085366	H_{42}	0.084826
C_9	-0.16817	H_{26}	0.085371	H_{43}	0.084855
C_{10}	-0.16814	H_{27}	0.0868	H_{44}	0.084865
C_{11}	-0.16808	H_{28}	0.086808	H_{45}	0.087973
C_{12}	-0.16862	H_{29}	0.084737	H_{46}	0.08798
C_{13}	-0.16721	H_{30}	0.084743	H_{47}	0.092229
C_{14}	-0.1591	H_{31}	0.085174	H_{48}	0.097694
C_{15}	-0.16904	H_{32}	0.085181	H_{49}	0.097706
C_{16}	-0.30775	H_{33}	0.084347	H_{50}	0.27528
O_{17}	-0.51046	H_{34}	0.084354	H_{51}	0.261727

H_{20} (0.131214) exhibiting the greatest positive charges. Hydrogen atoms are often less active in electron-sharing interactions. In addition to contributing to the molecule's overall polarity, the charges on hydrogen atoms close to nitrogen and oxygen also influence the molecule's reactivity in various chemical environments. A thorough comprehension of the electron density and possible reactive sites in the molecule is offered by the Mulliken charge distribution across HDA. The basis set and quantum mechanical approach options that are selected have an impact on these charges. To design and study a molecule's chemical reactivity and interactions with other species, researchers can forecast a molecule's behavior in electrophilic and nucleophilic reactions by examining its atomic charges.

Vibrational analysis

The maximum number of potentially active observable fundamentals for the linear molecule with N, C, H, and O atoms in C1 symmetry is (3N-6), excluding the three rotational and translational degrees of freedom [21]. There are 147 regular modes of vibration among the 51 atoms that make up the HDA molecule. With the use of the VEDA software and potential energy distribution (PED), the vibrational band allocations were determined. The comparison of observed and simulated FT-IR spectra is displayed in Fig. 3 [22]. In the lower frequency range of 1000–1300 cm^{-1}, a carbon–oxygen single bond (C–O) frequently experiences a stretching vibration. The CCC bond angle is formed when one carbon leaves the plane; this angle travels out of the plane and results in bending modes outside of it. These modes usually have a frequency in the 400–700 cm^{-1} range. Bending modes for C-C=O and H-C-C The H-C-C bond is frequently linked to bending vibrations that happen at lower frequencies, usually between 600 and 1200 cm^{-1}. Because HCC is

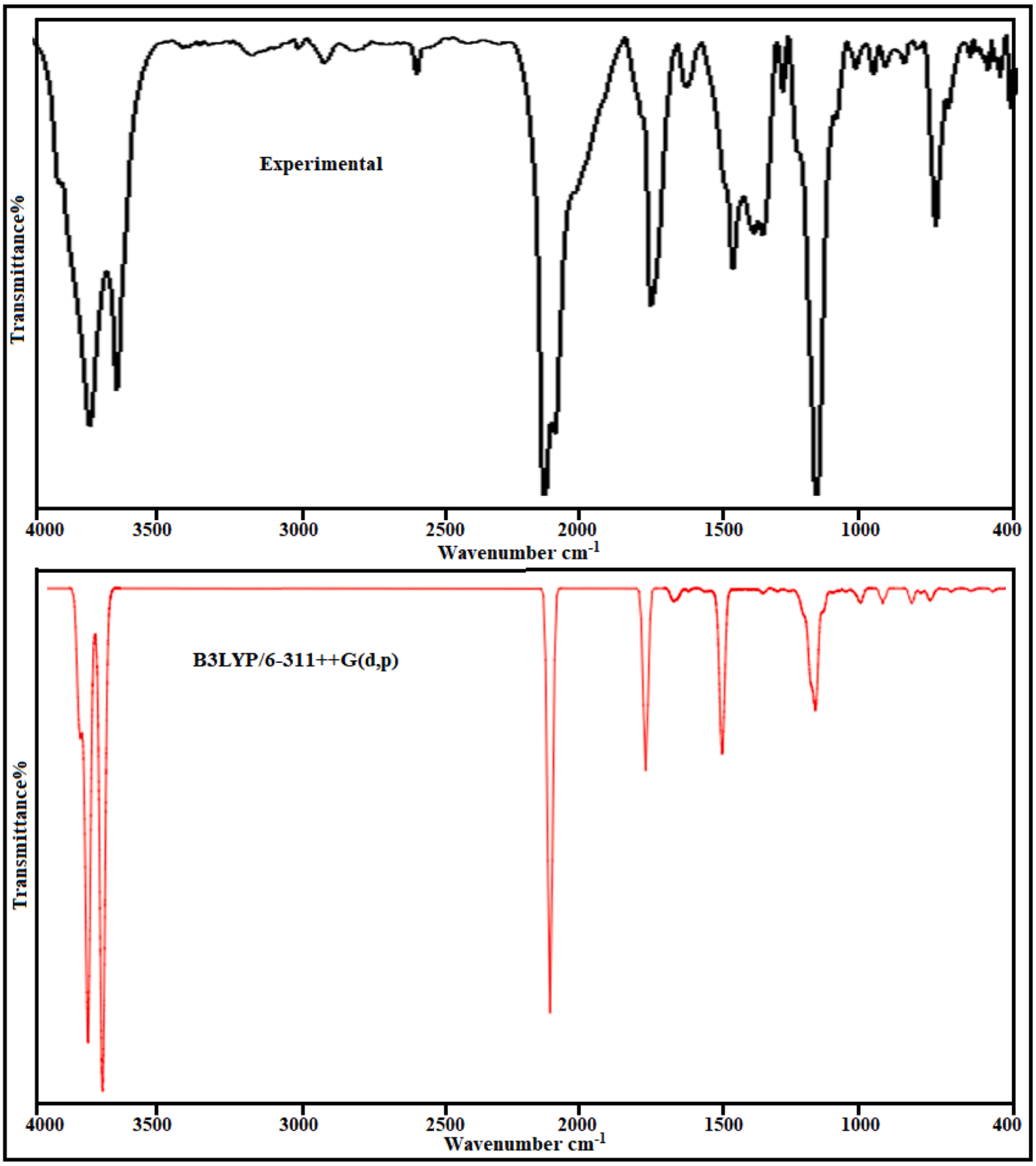

Fig. 3. FT-IR spectra compared with theoretical spectra on HDA molecules.

a radical species, its unique electrical structure and unpaired electron may result in frequency shifts and vibrational spectra that are somewhat different from those of stable molecules. To investigate these patterns, infrared spectroscopy and computational methods are frequently used [23–25]. 800–1200 cm^{-1} is the usual range for recording a σ-bond, C-C stretching vibration. The C=C stretching vibration commonly appears in the 1500–1700 cm^{-1} range when stretching in a π-bond. Various stretching and bending vibrations associated with the carbon-carbon bonds are part of the vibrational modes of the CCC (carbon--carbon-carbon) group, particularly in linear or cyclic structures. The 600–900 cm^{-1} range is commonly observed for the bending modes of the C-H bond in HCCC torsion and HCC bending. Since C-H stretching wavenumbers appear in aromatic compounds in the range of 3000–3100 cm^{-1}, this is the usual region for the rapid detection of C-H stretching vibrations. One of the hardest parts of infrared spectra to interpret is the C-H stretching and bending regions. The location and type of the substituent have no bearing on these vibrations. Nearly four infrared peaks in the 3080–3010 cm^{-1} range are present in most aromatic compounds due to ring C–H stretching bands. The B3LYP/6-311++G(d,P) method, before being compared to the experimental FT-IR data, the computed vibrational frequencies were scaled by a factor of 0.96. which is used in this study to observe various modes of stretching, bending, torsional, and out-of-plane vibrations at 1799, 633, 563, 1361, 1141, 3755, 1070, 1476, and 455. The results show good agreements with the vibrations observed in the experiments. The observed band in the recorded FT-IR spectra is 1788, 630, 569, 1360, 1138, 3751, 1070, 1478, and 450 cm^{-1}. The PED that corresponds to this pure mode of the title molecule contributed 82 %, 29 %, 59 %, 85 %, 12 %, 11 %, 14 %, 60 %, 10 %, 60 %, 63 %, 15 %, and 30 %, as indicated in Table 3.

Electronic properties of UV-visible spectroscopy

Using TD-DFT calculations at the B3LYP/6-311++G(d,p) level in the gas phase, water, and DMSO, the electronic absorption properties of HDA were examined. The results were compared with the experimental absorption band range between approximately 150 - 200 nm, and they are displayed in Fig. 4 and Table 4 [26,27]. In the gas phase, the first excited state (S1) appeared at 218.09 nm (5.68 eV) with a very weak oscillator strength (f = 0.0004), mainly attributed to HOMO → LUMO (95 %) with minor H-2 → LUMO contributions, while the S2 transition at

Table 3
Vibrational assignment.

B3LYP/6-311++G(d, p)	Experimental (cm^{-1})	Vibrational assignments +PED	B3LYP/6-311++G(d, p)	Experimental (cm^{-1})	Vibrational assignments +PED
3755	3751	υ NH (60)	1093	-	δ HNC (11) + υ NC (47) + δ HCC (14)
3613	3617	υ NH (39)	1070	-	υ CC (50)
3041	-	υ CH (17)	1074	-	υ CC (12)
3054	3056	υ CH (98)	1072	1070	υ CC (35)
3093	-	υ CH (44)	1069	-	υ CC (23)
3037	-	υ CH (35)	1068	-	υ CC (18)
3035	3039	υ CH (13)	1058	-	υ CC (13)
3033	-	υ CH (11)	1052	1053	υ CC (60)
3031	-	υ CH (38)	1036	-	υ CC (25)
3032	-	υ CH (14)	1020	-	υ CC (18)
3027	3022	υ CH (34)	1010	-	υCC (15)
3024	-	υ CH (12)	988	983	υCC (48)
3010	-	υ CH (24)	901	-	υCC (17) + τ HCCC (15)
3009	-	υ CH (26)	858	-	υNC(42) + υ CC(49)
3008	-	υ CH (12)	738	740	τ HCCC (12)
1799	1788	υ OC (82)	633	630	τHNCC(10) + τHCCN(14) + ${}_{\beta}$OCNC (29)
1623	-	δ HNH (11)	563	569	δ HNC (11) + δ CCC (17) + δ OCN (59)
1530	-	δ HCH (14)	533	-	δ CCC (30)
1523	-	δ HCH (24)	455	450	δ CCC (15)
1513	-	δ HCH (38) + τ HCCC (15)	428	422	δ CCC (30)
1500	-	δ HCH (28)	367	-	δ CCC (11)
1476	1478	δ HCH (63)	356	-	δ CCC (12)
1419	-	τ HCCC (12)	287	-	δ CCC (14)
1367	-	υ NH (91)	214	-	δ CCC (12)
1361	1360	υ NC (85) + υ CC (10) + δ HNC (11)	180	-	τ CCCC (29)
1352	-	δ HCC (22)	178	-	τ CCCC (30)
1351	-	δ HCC (19)	165	-	τ CCCC (29)
1348	1348	δ HCC (15)	143	-	τ CCCC (10)
1345	-	δ HCC (13)	137	-	τ CCCC (18)
1340	-	δ HCC (30)	107	-	τ CCCC (15)
1330	1333	δ HCC (11)	93	-	δ CCC (11)
1331	-	δ HCC (21)	67	-	τ CCCC (37)
1317	-	δ HCC (14)	48	-	δ CCC (11)
1141	1138	τ NCCC (12) + τ HCCC (18)	16	-	δ CCC (14)

δ -bending, υ- stretching, τ – twisting.

162.97 nm (7.61 eV, f = 0.0637) was dominated by H-1 → LUMO (70 %) along with HOMO → L+1 and HOMO → L+2 excitations, and the S3 state at 161.41 nm (7.68 eV) arose largely from H-2 → LUMO (88 %) with negligible oscillator strength, indicating weak optical activity. Solvent effects were minimal, with water showing almost identical values to the gas phase, whereas DMSO induced slight redshifts with S1 at 218.20 nm, S2 at 163.15 nm (f = 0.0661), and S3 at 161.15 nm, reflecting mild stabilization of charge redistribution due to its high polarity [28,29]. The experimental absorption band at 200 nm falls within the calculated excitation window of 161–218 nm, with the slight overestimation of the S1 state being typical of hybrid functional-based TD-DFT methods. The calculated range corresponds to π → π* and weak n → π* transitions associated with the amide group, where the strong S2 transition highlights the dominance of H-1 → LUMO excitations in the UV absorption profile, while S1 and S3 represent low-probability transitions. Overall, HDA exhibits absorption in the deep UV region, governed mainly by HOMO → LUMO and H-1 → LUMO excitations, with solvent polarity exerting only a minor effect and the experimental peak at 200 nm validating the computational predictions.

Molecular electrostatic potential

The electrostatic potential of molecules Charge distribution is visualized by MEP maps, which highlight the nucleophilic (blue) and electrophilic (red/yellow) reactive sites that control intramolecular and intermolecular interactions as shown in Fig. 5. Given that the interactions between neighbouring atoms are determined by their potential, the electrostatic potential [V (r)] can be used to quantify these interactions like V(r) – Electrostatic potential at point **r**, $\sum A$ – Summation over all nuclei, Z_R – Charge of nucleus, R_A – Position of nucleus, r – Position where the potential is calculated, ρ(r′) – Electron density at position, |r′−r| – Distance between electron element and observation point [30,31].

$$V(r) = \sum \frac{Z_R}{R_A - r} - \int \frac{\rho(r')}{(r' - r)} \tag{1}$$

For HDA, oxygen atoms show negative potential (nucleophilic sites), while hydrogen atoms display positive potential (electrophilic sites), with green indicating neutral regions. The MEP surface of HDA reveals distinct charge distributions that are directly relevant to its anticancer activity during docking studies. The negative potential regions (red, –1.183 × 10^{-2} a.u.) are localized around the carbonyl oxygen of the amide group, highlighting strong electron-rich zones that act as potential hydrogen bond acceptors and can positively interact with positively charged residues in protein active sites. Conversely, the positive potential regions (blue, +1.183 × 10^{-2} a.u.) are concentrated near the amide hydrogen atoms, indicating electron-deficient areas that function as hydrogen bond donors, enabling interactions with negatively charged residues like aspartate or glutamate. The green regions, representing nearly neutral potential, correspond primarily to the long alkyl chain, which provides a hydrophobic surface well-suited for stabilizing van der Waals and lipophilic interactions within nonpolar pockets of cancer-related proteins.

NBO analysis

The Natural Bond Orbital (NBO) analysis of HDA was performed using the NBO 3.1 program and the B3LYP/6-311++G (d, p) level of theory using Gaussian 09 W software. This research provides more insight into the molecule's electron density distribution and how

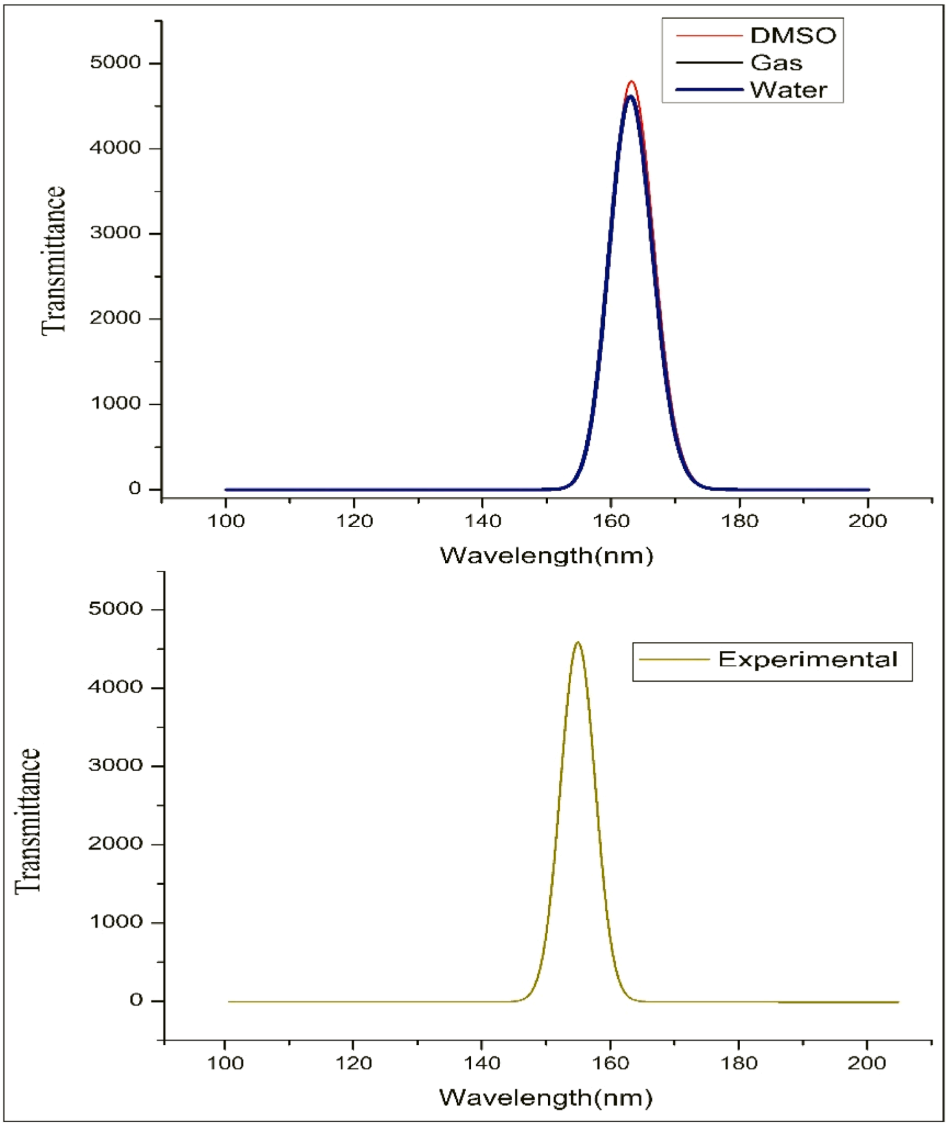

Fig. 4. UV–visible spectrum theoretical and experimental analysis.

rehybridization and donor-acceptor interactions impact its stability [32, 33]. The NBO approach has the advantage of offering data on interactions in both virtual and filled orbital regions, which could enhance the study of interactions within and between molecules. Identification of interactions between electron donors (bonding or lone pair orbitals) and acceptors (antibonding orbitals), which are important in stabilizing the molecule, is a crucial part of NBO analysis. The stabilization energy E (2) associated to the delocalization i/j for every donor (i) and acceptor (j) is computed as

$$E^{(2)} = \Delta E_{ij} = q_i \frac{F(i,j)^2}{\varepsilon_j - \varepsilon_i} \tag{2}$$

where the energy of the NBO donor and acceptor is represented by E_i and E_j, respectively, the orbital stabilization energy by E (2), the occupancy of the donating orbitals by q_i, and the Fock matrix element connecting NBO orbitals i and j by $F_{i,j}$. The stabilization energy, or E(2), quantifies the contribution of these interactions to the overall stability of the molecule. Higher E (2) values indicate stronger donor-acceptor interactions and greater electron delocalization, which ultimately increase molecule stability through hyperconjugation and resonance effects [34, 35]. Table 5 provides an overview of the calculated donor-acceptor interactions and significant stabilization energies of HDA. This study determined that the stabilization energy of the interaction between the antibonding σ* orbital of C_9-C_8 and the C_9-C_{10} σ bond was 23.26 kJ/mol. Significant electron transport of n→π* and σ→σ* transitions demonstrated here, which supports molecule stability. Furthermore, a noteworthy interaction with stabilization energies of 30.76 kJ/mol and 52.73 kJ/mol, respectively, was found between the lone pair on N_{17} and the π* antibonding orbitals of N_{17}-C_1 and C_1-O_{18}. The significance of nitrogen's lone pair in supporting electron delocalization and molecule stability is shown by these potent interactions. With a stabilization energy of 26.09 kJ/mol, the oxygen atom O_{18} lone pair also demonstrated notable stabilization through interaction with the C_1-C_2 π* orbital. The lone pair in oxygen plays a crucial function in improving the overall stability of the molecule, as this interaction indicates. The distribution of electron density and how donor-acceptor interactions support the stability of HDA are explained in detail by this NBO study. Understanding the behavior and stability of the molecule at the quantum chemical level depends on the substantial delocalization of electrons and hyperconjugation effects seen in these interactions.

Frontier molecular orbital (FMO) analysis

Frontier molecular orbitals (HOMO and LUMO) represent a

Table 4
Experimental & calculated absorption wavelength, energy, and oscillator strengths of HDA.

Solvents	States	B3LYP/6-311++G (d, p)			Major Contributions (%)
		Absorption band λ (nm)	Excitation energies (eV)	Oscillation Strength	
Gas Phase	**S1**	218.09	5.6848	0.0004	HOMO->LUMO (95 %), H-2->LUMO (4 %)
	S2	162.97	7.6077	0.0637	H-1->LUMO (70 %), HOMO->L + 1 (10 %), HOMO->L + 2.
	S3	161.41	7.6811	0.0000	H-2->LUMO (88 %) H-3->LUMO(6 %), HOMO->LUMO (4 %)
Water	**S1**	218.09	5.6848	0.0004	HOMO->LUMO (95 %), H-2->LUMO (4 %)
	S2	162.97	7.6077	0.0637	H-1->LUMO (70 %), HOMO->L + 1 (10 %), HOMO->L + 2.
	S3	161.41	7.6811	0.0000	H-2->LUMO (88 %) H-3->LUMO(6 %), HOMO->LUMO (4 %)
DMSO	**S1**	218.20	5.6819	0.0004	HOMO->LUMO (95 %) H-2->LUMO (3 %)
	S2	163.15	7.5991	0.0661	H-1->LUMO(70 %), HOMO->L + 1 (10 %) HOMO->L + 2
	S3	161.15	7.6850	0.0001	H-2->LUMO (89 %) H-3->LUMO (6 %), HOMO->LUMO (4 %)
Experimental		159	-	-	-

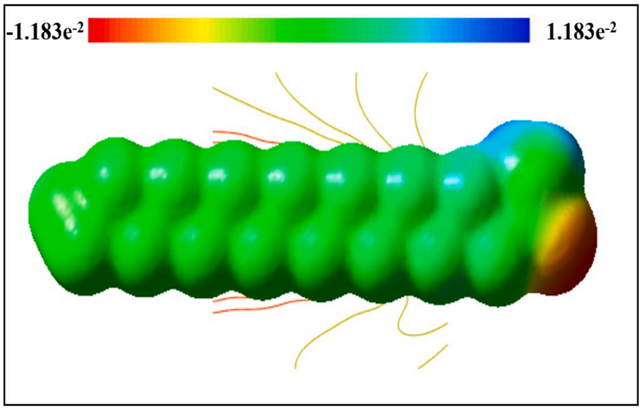

Fig. 5. MEP surface of HDA molecules.

molecule's capacity to give or take electrons, which contributes to its stability, reactivity, and electrical behavior. These qualities are crucial in applications including conductivity, biological activity, and solar cells. The electronic properties of the molecule, as determined by HOMO-LUMO analysis, indicate its promising potential for anticancer activity [34,35]. In Table 6 and Fig. 6 show HOMO energy is –6.53 eV, showing that the molecule's electrons are strongly bound and less likely to donate electrons, while the LUMO energy of 0.91 eV suggests that it can readily accept electrons from biomolecules, which is essential for interacting with cancer-related enzymes or DNA. The energy gap (ΔG) of 7.36 eV (calculated as LUMO – HOMO) implies chemical reactivity, allowing the molecule to participate in electron transfer reactions without being overly unstable. The ionization potential of 6.45 eV and electron affinity of –0.91 eV further highlight its tendency to hold onto electrons while also being able to form charge-transfer complexes. The chemical hardness of 3.68 eV and chemical softness of 0.14 eV^{-1} indicate that the molecule is soft and polarizable, enhancing its ability to interact with biological targets through non-covalent forces such as hydrogen bonds or π-stacking. With an electronegativity of 2.77 eV and chemical potential of -2.77 eV, the molecule demonstrates a tendency to lose electrons, potentially affecting redox processes within cancer cells. The electrophilicity index of –1.04 eV, despite its negative value likely due to computational scaling, conceptually suggests that the molecule can act as an electron acceptor, interfering with nucleophilic sites in cancer-associated biomolecules. Collectively, these properties suggest that the molecule may effectively engage in interactions that inhibit cancer cell growth.

Table 6
FMO analysis.

Parameters (eV)	Values
LUMO Energy	0.91
HOMO Energy	-6.53
Energy Gap (ΔG)	7.45
Ionization Potential (I)	6.45
Electron Affinity (A)	-0.91
Chemical Hardness (η)	3.68
Chemical Softness (S)	0.14
Electronegativity (χ)	2.77
Chemical Potential (μ)	-2.77
Electrophilicity Index (ω)	1.04

Table 5
Second-order perturbation theory analysis of Fock matrix in NBO.

Donor(i)	Type	ED/e	Acceptor(i)	Type	ED/e	E(2) (KJ mol^{-1})	E(J)-E(i) (a.u.)	F (i, j) (a.u.)
C_9-C_{10}	σ	1.6959	C_9-C_8	σ*	0.4373	23.26	0.32	0.079
			C_{11}-C_{10}	σ*	0.3570	18.65	0.31	0.069
			C_9-C_{10}	σ*	0.3412	24.07	0.32	0.079
C_{12}-H_{39}	σ	1.9729	C_{13}-C_{12}	σ*	0.0377	4.48	1.15	0.064
			C_{12}-C_{11}	σ*	0.0298	4.74	1.16	0.066
N_{17}	LP (1)	1.6904	N_{17}-C_1	π*	0.0272	30.76	0.29	0.086
			C_1-O_{18}	π*	0.3732	52.73	0.30	0.114
O_{18}	LP (2)	1.8841	C_1-C_2	π*	0.4373	26.09	0.38	0.097

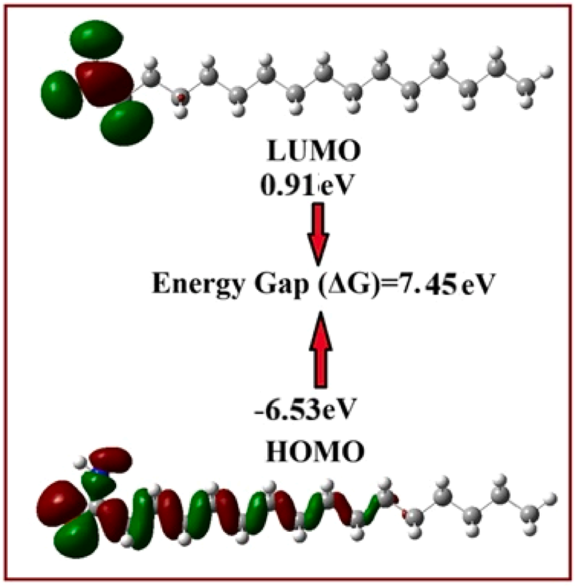

Fig. 6. Representation of HOMO-LUMO, energy gap, chemical stability & reactivity on HDA molecules.

Topological analysis

By the use of the Localized Orbital Locator (LOL) and Electron Localization Function (ELF) maps, the covalent bonding-based surface analysis offers vital information. These maps show areas of molecular space where electron pairs are most likely to be found [36,37]. The electron pair density is represented by ELF, which is represented by τ(r), and the maximum localized orbital overlap zones are highlighted by LOL, which is represented by η(r), because of the orbital gradients. In this investigation, Multiwfn 3.7 bin win64 was used to build both LOL and ELF maps. The electron pair distribution inside the molecule is clearly shown by the ELF map, whereas the degree of orbital localization is better understood by the LOL map. In particular, the LOL map of HDA (Fig. 7a and b) shows important locations for chemical bonding. Areas with greater LOL values, indicating localized electrons, are shown by red, orange, and yellow areas on the LOL color-filled plane map, whereas areas with lower LOL values, suggesting electron delocalization, are indicated by blue areas. Between 0.000 and 0.800 are the LOL values; locations with localized orbitals are indicated by higher ranking (red) values, while delocalized electron regions are indicated by lower values (blue). Furthermore, the depletion layer between the valence and inner shells is depicted in the ELF, which indicates regions where lone pairs may develop. The ELF (Fig. 7c and d) shows the values for HDA range from 0.000 to 1.000, where blue indicates lesser electron localization and red indicates higher localization. The ELF analysis also reveals that the molecule contains carbon atoms, as indicated by the blue patches that represent their locations. An important descriptor of chemical bonding in the molecule, showing regions of electron delocalization, is the topological route obtained from the LOL analysis. The analysis of the ELF and LOL values, which range from -20.9 to 20.9 Bohr, offers a thorough comprehension of the electron distribution in HDA and provides important information on its bonding properties and chemical reactivity.

Molecular docking

The interaction of HDA with the target protein 7QTZ was studied using AutoDock Tools 1.5.6 [38,39]. MolView was used to create the ligand structure, while the protein structure was obtained from the Protein Data Bank (PDB). Using the thermodynamic link between Gibbs free energy and the equilibrium constant, the inhibition constant (Ki) was calculated from the docking binding free energy:

$$\Delta G = RT \ln Ki \tag{3}$$

where T is the absolute temperature (298 K), R is the universal gas constant (1.987 cal mol^{-1} K^{-1}), Ki is the calculated inhibition constant, and ΔG is the binding free energy derived from the docking calculation. Using this relationship, the docking energy was used to calculate the Ki value reported in this study. Two hydrogen bonds with ASN 96 were formed, according to the docking data, with bond distances of 2.1 Å and 2.5 Å. The binding affinity between the ligand and the target protein was indicated by the docking calculation's binding free energy of −4.40 kcal/mol, which corresponds to an estimated inhibition constant (Ki) of roughly 590 µM.. A binding free energy of −4.40 kcal/mol was obtained from the docking calculation, indicating a weak to moderate binding affinity between the ligand and the target protein. As a result, the interaction reported in this study should be interpreted cautiously in terms of computational docking analysis. The docking analysis focused on the binding energy and hydrogen-bond interactions of the best-ranked docking pose. Overall, the docking data indicate that ASN 96 is the primary mediator of a stable contact between HDA and the target protein shown in Table 7 and Fig. 8(a–c). A Ramachandran plot, which examines the backbone dihedral angles (φ and ψ) of amino acid residues, was utilized to evaluate the stereochemical quality of the protein structure (7QTZ) employed for molecular docking. More than 90 % of residues are found in the favored regions, which correlate to energetically desirable conformations such α-helices and β-sheets, as seen in Fig. 8(c). Only a small percentage of residues are found in banned regions, whereas a smaller fraction of residues are found in additionally authorized regions. This distribution supports the protein structure's potential for molecular docking study by showing that it has adequate stereochemical quality and structural dependability. HDA's ADME prediction shows advantageous in silico pharmacokinetic characteristics. HDA is located inside the projected Blood–Brain Barrier (BBB) permeable region (yellow area) in the WLOGP vs. TPSA plot, indicating a potential capacity to penetrate the BBB in theory. Additionally, according to computational models, it is situated inside or close to the High Intestinal Absorption (HIA) region (white area), suggesting a probability of good intestinal absorption [40–42]. Additionally, HDA is anticipated to be PGP − (red circle), suggesting that P-glycoprotein efflux transporters may not use it as a substrate. Based on in silico ADME research, these results show desirable drug-likeness characteristics; however, they are predictive results that need to be validated experimentally to ensure biological relevance.

Mathematical aspects of compound

The different degree-based topological indices that have been computed to aid in the comprehension of molecular physical characteristics and chemical reactivity are highlighted in this section. Drug molecules are represented as molecular graphs in theoretical chemistry, with atoms standing in for vertices and bonds for edges. Edge partition data was used to derive topological descriptors for the compound under study. The molecular graph is composed of a set of atom-representing vertices (V(G)) and bond-representing edges (E(G)) [43]. The total number of edges and vertices in the molecular graph determines its size and order, respectively. The degree of each vertex, denoted by d(u) and d(v), indicates the number of bonds bonded to a particular atom. As illustrated in Fig. 9. the molecular structure is examined in this work using a range of degree-based topological indices [44].

Definition 1. Trinajestic and Gutman created the first and second Zagreb indices, M1 (G) and M2(G) [45]

$$M1(G) = \sum_{uv\in E(G)} (du + dv) \tag{4}$$

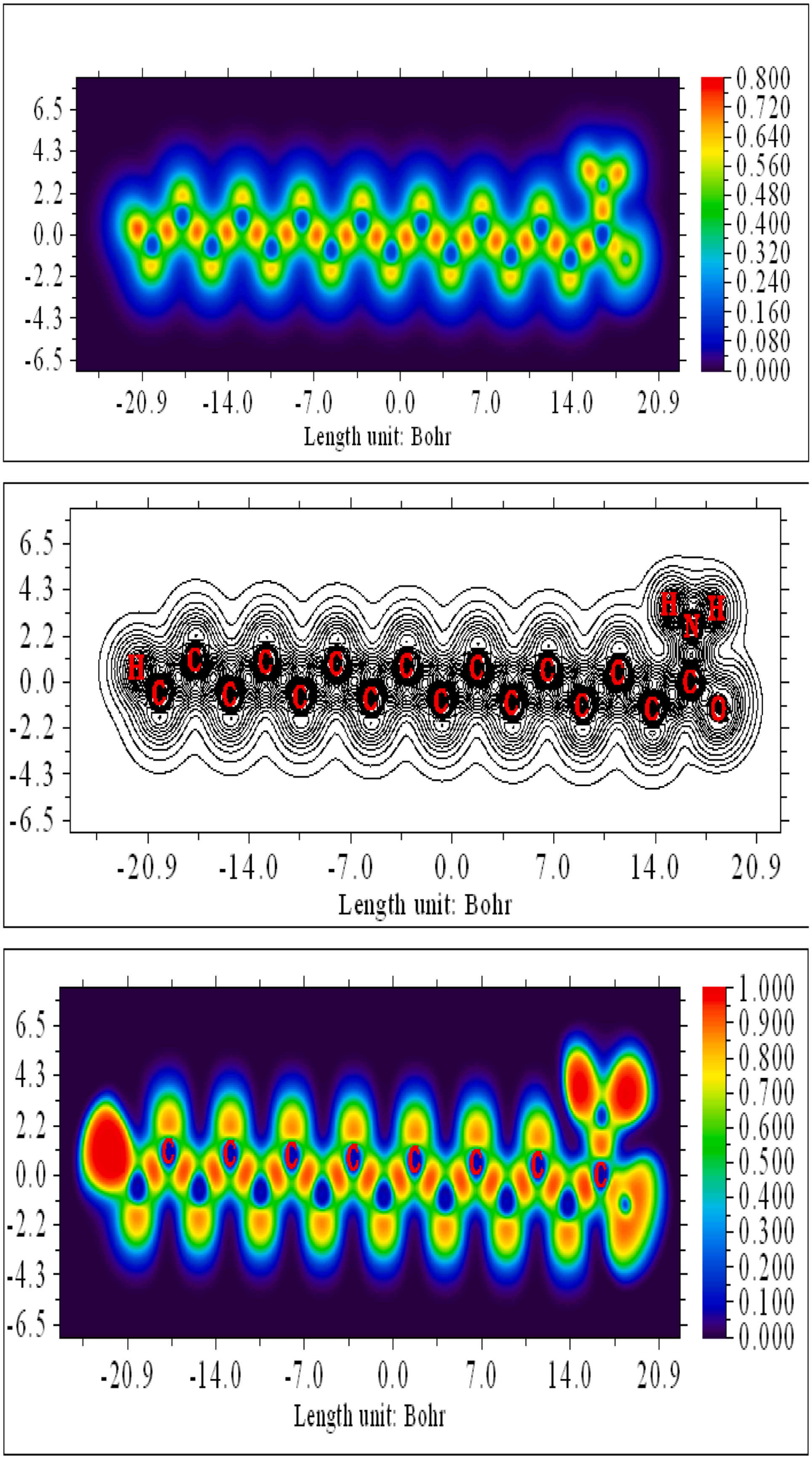

Fig. 7. (a). Localized orbital locator (LOL) map of HDA. (b). Localized orbital locator (LOL) Outline map of HDA. (c). Electron localized function (ELF) map of HDA. (d). Electron localized function (ELF) Outline map of HDA.

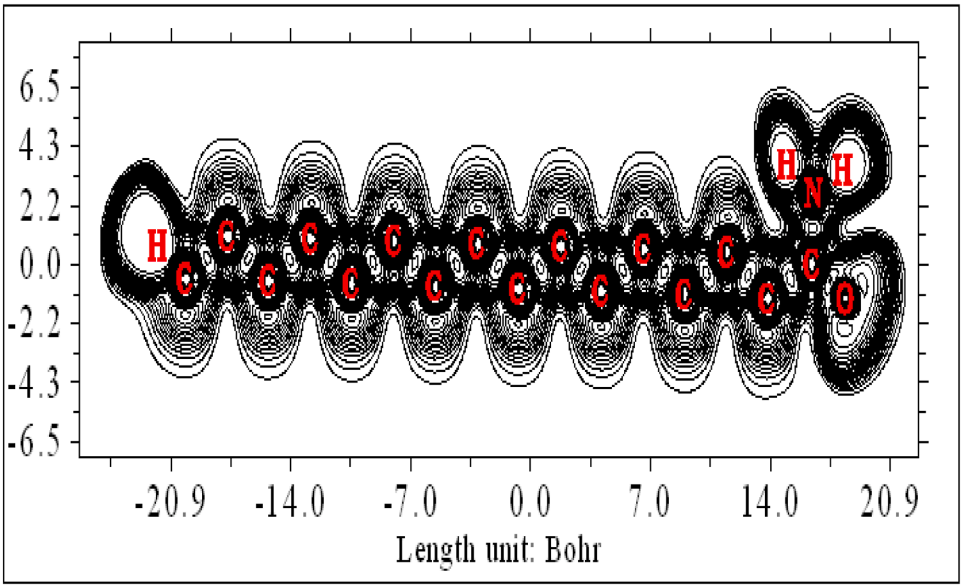

Fig. 7. (*continued*).

Table 7
The Binding affinity of the proteins with RMSD value on HDA.

Protein (PDB ID)	Bonded residues	No. of hydrogen bond	Bond distance (Å)	Estimated Inhibition Constant (µm)	Binding energy (kcal/mol)
7QTZ	ASN 96 (O...HN) ASN 96 (O…2HD2)	2	2.1 2.5	590	-4.40

and

$$M2(G) = \sum_{UV\in E(G)} (du.dv) \tag{5}$$

Definition 2. Harmonic index H(G) is [45] commuted as

$$H(G) = \sum_{UV\in E(G)} \frac{2}{du+dv} \tag{6}$$

Definition 3. explains the hyper Zagreb index [45] in the following way

$$HM(G) = \sum_{uv\in E(G)} (du+dv)^{2} \tag{7}$$

Definition 4. The Forgotten index F(G) [45] is described as

$$F(G) = \sum_{uv\in E(G)} \big[(du)^{2}\big| + \big|(dv)^{2}\big] \tag{8}$$

Definition 5. The following one provides the Reciprocal Randic Index RR(G) [45] in its entirety.

$$RR(G) = \sum_{uv\in E(G)} \sqrt{du\times dv} \tag{9}$$

Definition 6. As cited in [45], the Randic index RA(G) is shown below.

$$RA(G) = \sum_{uv\in E(G)} \sqrt{\frac{1}{du\times dv}} \tag{10}$$

Definition 7. The Sum Connectivity S(G) [45], which is shown by

$$S(G) = \sum_{uv\in E(G)} \sqrt{\frac{1}{du+dv}} \tag{11}$$

Definition 8. geometric-arithmetic (GA) index [45] is interpreted as

$$GA(G) = \sum_{uv\in E(G)} \frac{2\sqrt{du\times dv}}{du+dv} \tag{12}$$

Definition 9. Atom Bond Connectivity Index ABC (G) [45] is given below

$$ABC(G) = \sum_{uv\in E(G)} \sqrt{\frac{du+dv-2}{du\times dv}} \tag{13}$$

The edge partition techniques we obtained using the hydrogen depletion of HDA Fig. 9 were used to determine these degree-based topological indices.

Theorem The numerous degree-based topological indices of G, if G is the molecular graph of HDA molecules, are listed below [45].

M1(HDA) = 71, M2(HDA) = 66, H(HDA) = 10.3, HM(HDA) = 271, F (HDA) = 139, RR(HDA) = 35.64, RA(HDA) = 5.25, S(HDA) = 5.15, GA(HDA) = 12.36, ABC(HDA) = 9.

Proof. Let G be the HDA graph and let E(i,j) be the class of edges connecting vertices of degree i to degree j. Fig. 9. shows that |E 0,2| = 1, |E 1,2| = 3, and |E 2,2| = 15.

i) The following is the outcome of applying Definition 1: M1(HDA) $= 1(0+2) + 3(1+2) + 15\,(2+2) = 71$ and M2(HDA) $= 1(0\times 2) + 3(1\times 2) + 15(2\times 2) = 66$
ii) The following is the outcome of applying Definition 2: H(HDA) $= 1\times\frac{2}{0+2} + 3\times\frac{2}{1+2} + 15\times\frac{2}{2+2} = 10.3$

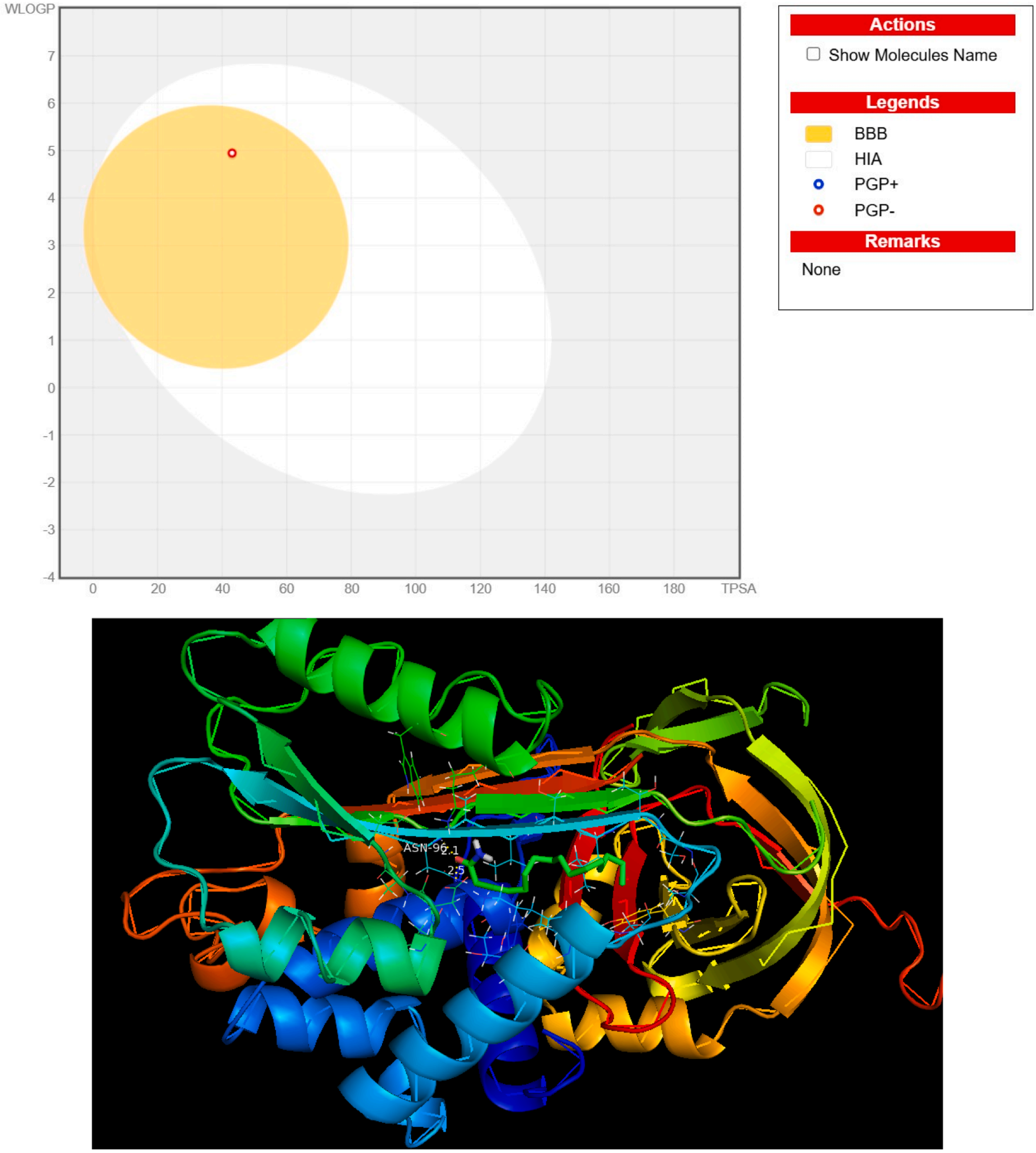

Fig. 8. (a). Boiled egg map for HDA. (b). Molecular docking studies of HDA with 7QTZ protein. (c). Ramachandra plot of HDA with 7QTZ protein.

iii) The following is the outcome of applying Definition 3: HM(HDA) $= 1x\ (0+2)^2 + 3\ (1+2)^2 + 15\ (2+2)^2 = 271$

iv) The result of using Definition 4 is as follows:

$$F(HDA) = 1[0^2 + 2^2] + 3[1^2 + 2^2] + 15\ [2^2 + 2^2]{=}139$$

v) The result of using Definition 5 is as follows:

$$RR(HDA) = 1\sqrt{0\ \times\ 2} + 3\sqrt{1\ \times\ 2} + 15\sqrt{2\ \times\ 2} = 35.64$$

vi) The result of using Definition 6 is as follows:

$$RA(HDA) = 1\ \times\ \sqrt{\frac{1}{0\times2}} + 3\ \times\ \sqrt{\frac{1}{1\times2}} + 15\sqrt{\frac{1}{2\ \times\ 2}} = 5.25$$

vii) The following is the outcome of applying Definition 7:

$$S(HDA) = 1\ \times\ \sqrt{\tfrac{1}{2}} + 3\ \times\ \sqrt{\tfrac{1}{3}} + 15\ x\ \sqrt{\tfrac{1}{4}} = 5.15$$

viii) The following is the outcome of applying Definition 8:

$$GA(HDA) = 1\left(\frac{2\sqrt{0\ \times\ 2}}{0+2}\right) + 3\left(\frac{2\sqrt{1\ \times\ 2}}{1+2}\right) + 15\left(\frac{2\sqrt{2\ \times\ 2}}{2+2}\right) = 12.36$$

ix) The following is the outcome of applying Definition 9:

$$ABC(HDA) = 1\sqrt{\frac{0+2-2}{0\ \times\ 2}} + 3\sqrt{\frac{1+2-2}{1\ \times\ 2}} + 15\sqrt{\frac{2+2-2}{2\ \times\ 2}} = 9$$

The Table 8 explain the corresponding values of the physical and mathematical relation exhibited the relation of **β** tot, m(D), Melting Point also corresponding to the values for the ABC(HDA) = 2.8 and F (HDA) = 211 value descriptors by QSPR analysis [45].

Conclusion

The identification of (HDA) from *Aegle marmelos* was examined through a combination of theoretical and experimental methods. The structural stability of the molecule was confirmed by DFT calculations at

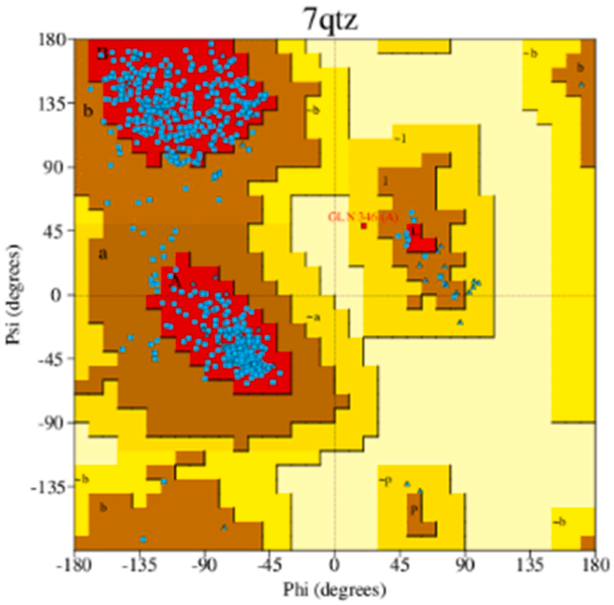

Fig. 8. (*continued*).

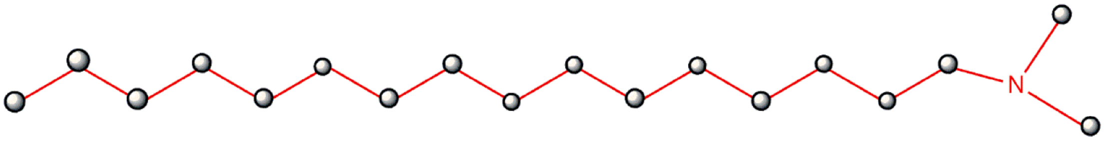

Fig. 9. QSPR analytical value of HDA.

Table 8
Physical and math comparative Of ZPSD.

S. No	Physical and chemical properties	Physical and chemical properties values	Mathematical QSPR analytical value.
1	**XLogP3**	5.7	S(HDA) = 5.15
2	**m/z 2nd Highest**	72	M1(HDA) = 71

the B3LYP/6-311++G(d,p) level, which produced optimized geometrical parameters with good agreement with experimental data. The experimental spectrum was validated and the fundamental modes were reliably assigned thanks to the scaled FT-IR vibrational frequencies and potential energy distribution (PED). The accuracy of the electronic transition analysis was confirmed by the TD-DFT results, which demonstrated a strong correlation with the experimental UV–visible absorption bands. While solvent effects showed increased electronegativity in aqueous media, the global reactivity descriptors showed chemical hardness and stability. The molecular electrostatic potential (MEP) surface revealed nucleophilic areas close to the amide nitrogen and electrophilic areas surrounding the carbonyl oxygen. Significant charge delocalization through N17-C1 $\pi^* \rightarrow$ C1–O18 π^*; n(O)/n(N) $\rightarrow \pi^*$ (C = O) interactions was confirmed by NBO analysis, which aided in electronic stabilization energy of 1.6904 kcal.mol^{-1}. Through hydrophobic and hydrogen bonding interactions, molecular docking showed that HDA bound favourably to the target protein. All things considered, the combined spectroscopic, quantum chemical, and docking data point to HDA as a structurally sound and physiologically significant molecule with room for more pharmacological research.

CRediT authorship contribution statement

G. Revathi: Writing – original draft. **P. Rajesh:** Visualization, Validation, Supervision, Software, Methodology, Conceptualization. **S. Kayashrini:** Visualization, Software. **S. Bala Abirami:** Investigation, Formal analysis.

Declaration of competing interest

The authors declare that they have no known competing financial interests or personal relationships that could have appeared to influence the work reported in this paper.

Data availability

Data will be made available on request.

References

[1] Chain F, Iramain MA, Grau A, Catalán CA, Brandán SA. Evaluation of the structural, electronic, topological and vibrational properties of N-(3, 4-dimethoxybenzyl)-hexadecanamide isolated from Maca (Lepidium meyenii) using different spectroscopic techniques. J Mol Struct 2017;1128:653–64.

[2] Kattelus J, Velasco JA, Auvinen P, Arandia A, Verkama E, Meinander K, Puurunen RL. Hydrodeoxygenation and hydrodenitrogenation of n-hexadecanamide with supported NiMo sulfide catalysts. Top Catal 2025:1–14.

[3] Hung AM, Mousavi M, Pahlavan F, Fini EH. Intermolecular interactions of isolated bio-oil compounds and their effect on bitumen interfaces. ACS Sustain Chem Eng 2017;5(9):7920–31.

[4] Narayanan A, Das D, Marimuthu M, Vasu G, Mani A, Subhadra R. In vitro cytotoxicity and wound healing activities of quaternary blended carboxymethyl cellulose-hydroxypropyl methylcellulose composite film. Cellulose 2024;31: 2295–308. https://doi.org/10.1007/s10570-023-05707-6.

[5] D'Souza UP, KSC RS, Pai V. GCMS analysis of bioactive compounds and evaluation of anti-parkinson activity of leaf extract of curculigo orchioides in ExperimentalAnimals. Curr Bioact Compd 2024;20. https://doi.org/10.2174/0115734072285993240403110533.

[6] Alam MJ, Ahmad S. Molecular structure, anharmonic vibrational analysis and electronic spectra of o-, m-, p-iodonitrobenzene using DFT calculations. J Mol Struct 2014;1059. https://doi.org/10.1016/j.molstruc.2013.12.002.

[7] Sundaraganesan N, Ayyappan S, Umamaheswari H, Joshua BDominic. FTIR,FT-raman spectra and ab initio, DFT vibrational analysis of 2,4-dinitrophenylhydrazine. Spectrochim Acta A 2007;66. https://doi.org/10.1016/j.saa.2006.02.015.

[8] Frisch MJ, Trucks GW, Schlegel HB, Scuseria GE, Robb MA, Cheese-man JR, Scalmani G, Barone V, Mennucci B, Petersson GA, Nakatsuji H, Caricato M, Li X, Hratchian HP, Izmaylov AF, Bloino J, Zheng G, Son-nenberg JL, Hada M, Ehara M, Toyota K, Fukuda R, Hasegawa J, Ishida M, Nakajima T, Honda Y, Kitao O, Nakai H, Vreven T, Montgomery Jr JA, Peralta JE, Ogliaro F, Bearpark M, Heyd JJ, Brothers E, Kudin KN, Staroverov VN, Kobayashi R, Normand J, Raghavachari K, Rendell A, Bu-rant JC, Iyengar SS, Tomasi J, Cossi M, Rega N, Millam JM, Klene M, Knox JE, Cross JB, Bakken V, Adamo C, Jaramillo J, Gomperts R, Stratmann RE, Yazyev O, Austin AJ, Cammi R, Pomelli C, Ochterski JW, Martin RL, Mo-rokuma K, Zakrzewski VG, Voth GA, Salvador P, Dannenberg JJ, Dapprich S, Daniels AD, Farkas O, Foresman JB, Ortiz JV, Cioslowski J, Fox DJ. Gaussian 09, Revision E.01. Wallingford CT: Gaussian, Inc.; 2009. p. 214–8.] program together with 6-31G(d, p) basis set function of the density functional theory (DFT) utilizing gradient geometry optimization [H.B. Schlegel, J. Comput. Chem. 3 (1982).

[9] Jamroz MH. Vibrational Energy Distribution Analysis, 4. Warsaw: VEDA; 2004.

[10] Lu Tian, Chen Feiwu. Multiwfn: A multifunctional wavefunction analyzer. J Comput Chem 2012;33:580–92. https://doi.org/10.1002/jcc.22885.

[11] Imtiaz F, Saif Z, Sajid A, Nazir A, Manzoor Q, Saleem A, Farooq A, Al-Mijalli SH, Iqbal M. Role of glycerol-based deep eutectic solvents for extraction of phytochemicals from Cichorium intybus seeds: optimization by response surface methodology. Microchem J 2024;199:110083. https://doi.org/10.1016/j.microc.2024.110083.

[12] Abubaker MA, Mohammed AAA, Farah AAM, Zhang J. Phytochemical screening by using GC-MS and FTIR spectrum analysis of fixed oil from Sudanese Ziziphus spina Christi seeds. Eur Chem Commun 2021;3. https://doi.org/10.22034/ecc.2021.273055.1137.

[13] de Sousa BCM, do A Gomes D, da S Viana AF, da Silva BA, Barata LES, Sartoratto A, Lustosa DC, Vieira TA. Phytochemical analysis and antioxidant activity of ethanolic extracts from different parts of dipteryx punctata (S. F. Blake). AmshoffAppl Sci (Switz) 2023;13. https://doi.org/10.3390/app13179600.

[14] E. Dhanalakshmi, P. Rajesh, K. Arunkumar, T. Gnanasambandan, Noureddine ISSAOUI, K. Sudha, M. Raja, Synthesis, GCMS, spectroscopic, electronic properties, chemical reactivity.

[15] RDG, topology and biological assessment of 1-(3,6,6-trimethyl-1,6,7,7a-tetrahydrocyclopenta[c]pyran-yl)ethenone. Chem Phys Impact 2023;7. https://doi.org/10.1016/j.chphi.2023.100385.

[16] He YJ, Xie MH, Zou P, Liu YL, Wu J. 3,3,12,12-Tetra-methyl-1,5,10,14-tetra-oxa-dispiro-[5.2.5.2]hexa-deca-ne. Acta Crystallogr E: Struct Rep Online 2009;65(7). https://doi.org/10.1107/S1600536809021291.

[17] Yadav B, Yadav RK, Srivastav G, Yadav RA. Experimental Raman, FTIR and UV-vis spectra, DFT studies of molecular structures and barrier heights, thermodynamic functions and bioactivity of kaempferol. J Mol Struct 2022;1258. https://doi.org/10.1016/j.molstruc.2022.132637.

[18] Allen FH. The geometry of small rings—IV. Tetrahedron 1982;38(5). https://doi.org/10.1016/0040-4020(82)80206-8.

[19] Dhanalakshmi E, Rajesh P, Kandan P, Kesavan M, Jayaraman G, Selvaraj A, Priya R. Stability of bonds, kinetic stability, energy parameters, spectral characterization, GC–MS and molecular descriptors studies on coumarine, 3-[2-(1-*methyl-2-imidazolylthio*)-1-*oxoethyl*]. J Mol Struct 2024;1295. https://doi.org/10.1016/j.molstruc.2023.136544.

[20] Sundaram S, Vijayakumar VN, Balasubramanian V. Electronic and structure conformational analysis (HOMO-LUMO, MEP, NBO, ELF, LOL, AIM) of hydrogen bond binary liquid crystal mixture: DFT/TD-DFT approach. ComputTheorChem 2022;1217. https://doi.org/10.1016/j.comptc.2022.113920.

[21] Anand G, Sivasubramanian M, Manimehan I, Ruby A, Abinayashri R, Asmitha RK. Synthesis, spectroscopic elucidation (FT-IR, FT-Raman, UV–vis), quantum chemical computation (PES, FMO, HOMO–LUMO, MEP, NLO, Hirshfeld) and molecular docking studies on 2-thiophenecarboxamide crystal. J Mol Struct 2023;1286. https://doi.org/10.1016/j.molstruc.2023.135586.

[22] Hung AM, Pahlavan F, Shakiba S, Chang SL, Louie SM, Fini EH. Preventing assembly and crystallization of alkane acids at the silica–bitumen interface to enhance interfacial resistance to moisture damage. Ind Eng Chem Res 2019;58(47):21542–52.

[23] Carron, K. T. (1998). *Site-selective spectroscopy of adsorbates on mineral surfaces using FTIR* (No. TR531862).

[24] Minteguiaga M, Dellacassa E, Iramain MA, Catalán CA, Brandán SA. Synthesis, spectroscopic characterization and structural study of 2-isopropenyl-3-methyl-phenol, carquejiphenol, a carquejol derivative with potential medicinal use. J Mol Struct 2018;1165:332–43.

[25] Li F, Katz L, Hu Z. Adsorption of major nitrogen-containing components in microalgal bio-oil by activated carbon: equilibrium, kinetics, and ideal adsorbed solution theory (IAST) model. ACS Sustain Chem Eng 2019;7(19):16529–38.

[26] Sonia Chiging, Devi ThGomti, Karlo T. Study of isoniazid-pyridoxine biomolecular complex using spectroscopic (Raman, SERS, FTIR, UV-vis) and quantum chemical calculation. J Mol Struct 2023;1292. https://doi.org/10.1016/j.molstruc.2023.136087.

[27] Lawrence M, Rajesh P, Thirunavukkarasu M, Muthu S. Solute-solvent interactions, electrostatic & covalent surface analysis, and pharmacokinetic studies via in-silico simulation on diethyl 3-hydroxyglutarate: anti-hypercholesterolemia activity. J MOL LIQ 2023;382. https://doi.org/10.1016/j.molliq.2023.121940.

[28] Kim TY, Kim JM, Lee HL, Go MJ, Joo SG, Kim JH, Heo HJ. Codium fragile suppressed chronic pm2. 5-exposed pulmonary dysfunction via TLR/TGF-β pathway in BALB/c mice. Antioxidants 2023;12(9):1743.

[29] Bungaran B, Ferdinand S. Exploring nanoherbal tomato: assessing its potential as an α-glucosidase and α-amylase inhibitor, antioxidant and metabolite profiling using LC-HRMS. Res J Pharm Technol 2024;17(10):4953–60.

[30] Ojha JK, Ramesh G, Reddy BV. Structure, chemical reactivity, NBO, MEP analysis and thermodynamic parameters of pentamethyl benzene using DFT study. Chem Phys Impact 2023;7. https://doi.org/10.1016/j.chphi.2023.100280.

[31] Politzer P, Murray JS. The molecular electrostatic potential: an overview. Theor Chem Acc 2002;108(3):134–42. https://doi.org/10.1007/s00214-002-0363-9.

[32] Alam M, Park S. Molecular structure, spectral studies, NBO, HOMO–LUMO profile, MEP and Mulliken analysis of 3β,6β-dichloro-5α-hydroxy-5α–cholestane. J Mol Struct 2018;1159. https://doi.org/10.1016/j.molstruc.2018.01.043.

[33] Mumit MA, Pal TK, Alam MA, Islam MAAAA, Paul S, Sheikh MC. DFT studies on vibrational and electronic spectra, HOMO–LUMO, MEP, HOMA, NBO and molecular docking analysis of benzyl-3-N-(2,4,5-trimethoxyphenylmethylene) hydrazine carbodithioate. J Mol Struct 2020;1220. https://doi.org/10.1016/j.molstruc.2020.128715.

[34] Kanchana S, Kaviya T, Rajkumar P, Kumar MD, Elangovan N, Sowrirajan S. Computational investigation of solvent interaction (TD-DFT, MEP, HOMO-LUMO), wavefunction studies and molecular docking studies of 3-(1-(3-(5-((1-methylpiperidin-4-yl)methoxy)pyrimidin-2-yl)benzyl)-6-oxo-1,6-dihydropyridazin-3-yl)benzonitrile. Chem Phys 2023;7. https://doi.org/10.1016/j.chphi.2023.100263.

[35] Mumit MA, Pal TK, Alam MA, Islam MAAAA, Paul S, Sheikh MC. DFT studies on vibrational and electronic spectra, HOMO–LUMO, MEP, HOMA, NBO and molecular docking analysis of benzyl-3-N-(2,4,5-trimethoxyphenylmethylene) hydrazinecarbodithioate. JMolStruct 2020;1220. https://doi.org/10.1016/j.molstruc.2020.128715.

[36] Sundaram S, Vijayakumar VN, Balasubramanian V. Electronic and structure conformational analysis (HOMO-LUMO, MEP, NBO, ELF, LOL, AIM) of hydrogen bond binary liquid crystal mixture: DFT/TD-DFT approach. ComputTheorChem 2022;1217. https://doi.org/10.1016/j.comptc.2022.113920.

[37] Sundaram S, Vijayakumar VN, Balasubramanian V. Electronic and structure conformational analysis (HOMO-LUMO, MEP, NBO, ELF, LOL, AIM) of hydrogen bond binary liquid crystal mixture: DFT/TD-DFT approach. ComputTheorChem 2022:1217. https://doi.org/10.1016/j.comptc.2022.113920.

[38] Lawrence M, Rajesh P, Thirunavukkarasu M, Muthu S. Solute-solvent interactions, electrostatic & covalent surface analysis, and pharmacokinetic studies via in-silico simulation on diethyl 3-hydroxyglutarate: anti-hypercholesterolemia activity. J MOL LIQ 2023;382. https://doi.org/10.1016/j.molliq.2023.121940.

[39] Mahajan M, Suryavanshi S, Bhowmick S, Alasmary FA, Almutairi TM, Islam MA, Kaul-Ghanekar R. Matairesinol, an active constituent of HC9 polyherbal formulation, exhibits HDAC8 inhibitory and anticancer activity. Biophys Chem 2021;273:106588. https://doi.org/10.1016/j.bpc.2021.106588.

[40] Dadashpour M, Firouzi-Amandi A, Pourhassan-Moghaddam M, Maleki MJ, Soozangar N, Jeddi F, Nouri M, Zarghami N, Pilehvar-Soltanahmadi Y. Anticancer potential of vernonia cinerea mediated AgNPs against the Human pancreatic cancer PANC. Mater Sci Eng: C 2018;92:902–12. https://doi.org/10.33745/ijzi.2023.v09i02.029.

[41] Kirsch DG, Kastan MB. Tumor-suppressor p53: implications for tumor development and prognosis. J Clin Oncol 1998;16(9):3158–68.

[42] Yuan C, Wang MH, Wang F, Chen PY, Ke XG, Yu B, Wu HZ. Network pharmacology and molecular docking reveal the mechanism of Scopoletin against non-small cell lung cancer. Life Sci 2021;270:119105.

[43] Furtula B, Gutman I. A forgotton topological index. J Math Chem 2015;53:213–20. https://doi.org/10.1007/s10910-015-0480-z.

[44] Gutman Ivan, Furtula Boris, Elphick Clive. Three new/old Vertex-degree-based topological indices. Commun Math Comput Chem 2014;72. https://www.researchgate.net/publication/279602396.

[45] Farahani Mohammad Reza. On the Randic and Sum-connectivity index of nanotubes. Ann West Univ Timis-Math Comput Sci 2013;51:39–46. https://doi.org/10.2478/awutm-2013-0014.